

Transport of a single cold ion immersed in a Bose-Einstein condensate

T. Dieterle,¹ M. Berngruber,¹ C. Hölzl,¹ R. Löw,¹ K. Jachymski,² T. Pfau,¹ and F. Meinert¹

¹*Physikalisches Institut and Center for Integrated Quantum Science and Technology, Universität Stuttgart, Pfaffenwaldring 57, 70569 Stuttgart, Germany*

²*Faculty of Physics, University of Warsaw, Pasteura 5, 02-093 Warsaw, Poland*

(Dated: May 30, 2022)

We investigate transport dynamics of a single low-energy ionic impurity in a Bose-Einstein condensate. The impurity is implanted into the condensate starting from a single Rydberg excitation, which is ionized by a sequence of fast electric field pulses aiming to minimize the ion's initial kinetic energy. Using a small electric bias field, we study the subsequent collisional dynamics of the impurity subject to an external force. The fast ion-atom collision rate, stemming from the dense degenerate host gas and the large ion-atom scattering cross section, allows us to study a regime of frequent collisions of the impurity within only tens of microseconds. Comparison of our measurements with stochastic trajectory simulations based on sequential Langevin collisions indicate diffusive transport properties of the impurity and allows us to measure its mobility. Furthermore, working with a free and untrapped ion provides unique means to distinguish single realizations, where the impurity is subject to inelastic molecular-ion formation via three-body recombination. We study the cold chemistry of these events and find evidence for subsequent rovibrational quenching collisions of the produced molecule. Our results open a novel path to study dynamics of charged quantum impurities in ultracold matter.

I. INTRODUCTION

Unraveling the microscopic details of transport processes forms a prime challenge to understand macroscopic phenomena in complex many-body systems. Paradigms thereof comprise Drude-type electronic motion, Cooper-pairing in superconductors, or hopping dynamics in lattice or spin systems. The advent of ultracold atomic gases has opened exciting new routes to perform microscopy of transport phenomena in quantum systems [1, 2], even at the level of individual particles by deliberately implanting single impurity atoms in the host gas and monitoring their dynamics in real time. Recent advances in controlling neutral impurities interacting with bulk Bose and Fermi gases, for example, offer means to investigate polaron formation [3–6], to trace individual particle collisions [7], or to study exotic impurity dynamics in reduced dimensions [8, 9]. Neutral impurities interact with the quantum gas via short-range contact interaction. In contrast, hybrid platforms combining neutral atoms with co-trapped ions allow for realizing strongly coupled charged impurities, which interact with the host gas via a comparatively long-range polarization potential [10].

The strong ion-atom interaction has been exploited not only for sympathetic collisional cooling of the ionic impurity by its host gas [11–14], but also for extensive studies of cold two- and three-body charge-neutral chemistry induced by the long-range tail of the polarization potential [15–18]. Further, the rich interplay between elastic collisions and chemical processes has been subject to theoretical studies of ionic impurities at ultralow temperatures, predicting coherent formation of exotic mesoscopic molecular ions with large effective masses [19, 20], or novel transport processes driven by resonant charge exchange [21]. Indeed, mobility studies of ions in liquid Helium have been exploited early on to probe central properties of superfluidity [22, 23]. However, the experimental realization of directed impurity transport in a cold ion-atom hybrid system so far remained elusive and is impeded by the presence of strong confining potentials and typical intrinsic

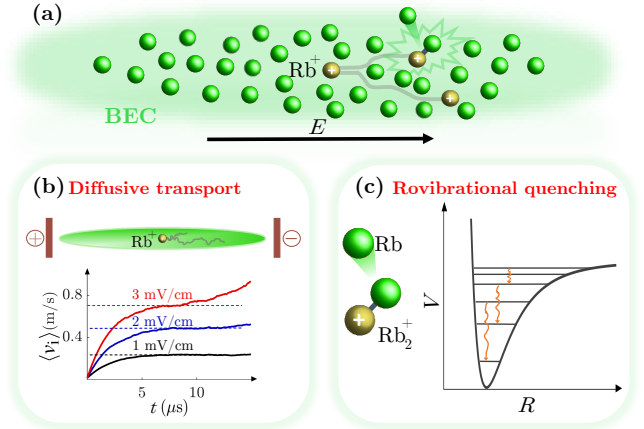


FIG. 1. (a) Schematic view of a single Rb^+ ion (yellow sphere) transported through a Bose-Einstein condensate via an applied electric field E . Two exemplary ion trajectories indicate frequent binary Langevin scattering with host gas atoms (green spheres) and a competing three-body collision event. (b) Numerical trajectory simulations (see text) of the mean velocity $\langle v_i \rangle$ as a function of evolution time t for an ion created at the BEC center predict a field-dependent drift velocity (dashed horizontal lines) after an initial transient, indicative of diffusive ion transport. (c) Two-body elastic scattering competes with three-body collision events resulting in the formation of weakly bound Rb_2^+ molecular ions, which may be quenched to more deeply bound rovibrational states in the molecular-ion potential $V(R)$ via secondary atom-molecule collisions.

trap-induced micromotion.

In this work, we study transport of a single cold ion through a Bose-Einstein condensate (BEC) on a completely different experimental footing. We control a free and low kinetic energy ionic impurity in the absence of any confining potentials. This ion is generated from a single precursor Rydberg atom by a tailored pulsed field-ionization sequence, and strong Rydberg blockade grants the creation of a single charged impurity only [24, 25]. Subsequently, we steer the ion through the

Bose-Einstein condensate by applying exquisitely controlled bias electric fields (Fig. 1). This allows us to observe indications of diffusive ionic transport as a result of the large cross section for ion-atom Langevin collisions. Importantly, we can distinguish transport due to elastic scattering from competing inelastic chemical reactions exploiting time of flight mass spectrometry. The latter cause the formation of weakly bound molecular ions, which we find to undergo subsequent atom-molecule rovibrational quenching collisions.

II. IONIC TRANSPORT THROUGH A BOSE-EINSTEIN CONDENSATE

The interaction between an ion and neutral atoms at long range is well captured by an induced charge-dipole polarization potential of the familiar form $V(R) = -C_4/(2R^4)$ [10], where R denotes the internuclear separation and C_4 the atom's polarizability ($C_4 = 318.8$ a.u. for Rb [26]). For the typical collision energies considered in this work, it is this long-range tail which determines the rate $\chi_L = 2\pi n_{\text{at}} \sqrt{C_4/\mu}$ of binary ion-atom scattering events leading to large deflection angles [27]. Here μ is the ion-atom reduced mass and n_{at} denotes the atom number density of the host gas. We start our discussion with the observation that the rate for such Langevin-type collisions can reach up to hundreds of kHz at densities typical for gaseous BECs ($n_{\text{at}} \sim 10^{14} \text{cm}^{-3}$), and may thus lead to frequent collisions on timescales of only a few tens of microseconds. Such fast scattering rates form the basis for our experiments and specifically allow us to observe collision-dominated transport dynamics of a free and untrapped ion controlled by small electric bias fields.

All our experiments start with the production of an elongated BEC of typically 8×10^5 ^{87}Rb atoms prepared in the $|5S_{1/2}, F=2, m_F=2\rangle$ hyperfine state and held in a magnetic QUIC trap with trap frequencies $(\omega_x, \omega_y, \omega_z) = 2\pi \times (194, 16, 194)$ Hz. This yields a condensate with corresponding Thomas-Fermi radii of $(4.4, 53, 4.4)$ μm and a peak density of $n_{\text{at}} = 4.1 \times 10^{14} \text{cm}^{-3}$. The BEC is surrounded by three pairs of electrodes [Fig. 2(b)], which allow us to control electric fields at the gas position to a level $\lesssim 300 \mu\text{V/cm}$ [25]. Next, we implant a single low-energy Rb^+ ion into the central region of the condensate. To this end, we promote one atom from the atomic ensemble to a highly excited $160S_{1/2}$ Rydberg level using a 500 ns long two-photon excitation pulse incorporating the intermediate $6P_{3/2}$ state at a detuning of +320 MHz. To account for density-induced level shifts of the Rydberg line in the BEC, the lasers are detuned by -40 MHz from the bare Rydberg state energy [24]. One of the excitation lasers is focused into the condensate center through a high-NA aspheric lens to a beam waist of about $1.8 \mu\text{m}$, providing excellent spatial control over the position of the created Rydberg atom. Note that strong Rydberg blockade inhibits more than one excitation at a time. Subsequently, the single Rydberg atom is ionized by a short (10 ns long) electric field pulse of 2.85V/cm . We counteract the rapid acceleration of the ion induced by the ionization field with a second tailored field pulse of similar shape but with opposite polarity. This sequence

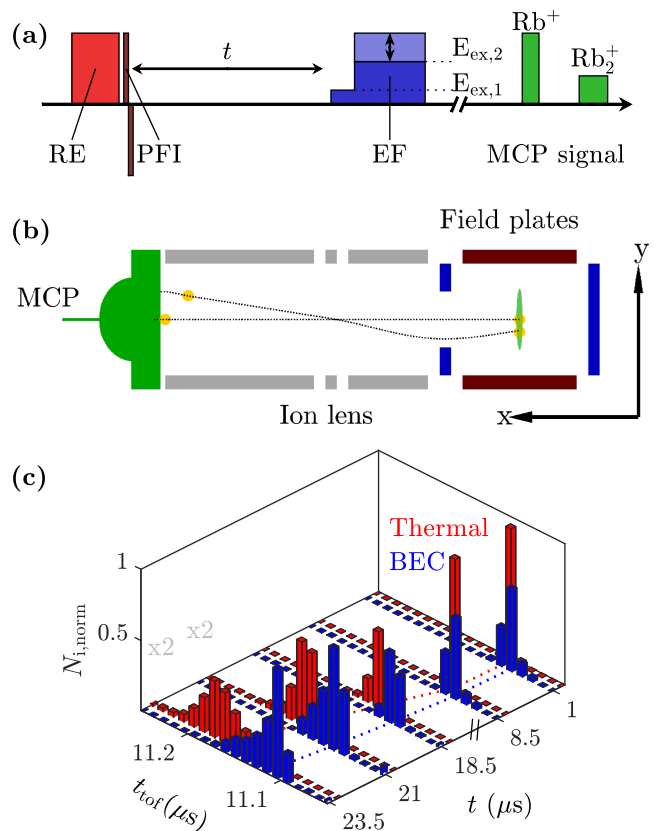


FIG. 2. (a) Measurement sequence consisting of the excitation of a single Rydberg atom (RE) and production of a low-energy ion via pulsed field ionization (PFI). After a variable evolution time t in the electric field E , a two-step electric field pulse (EF) guides the ion to the MCP for temporarily separated detection of Rb^+ and Rb_2^+ . (b) Detection principle of ionic transport. The two-step extraction pulse (EF in (a)) in combination with an ion lens in einzel lens configuration results in a time of flight to the MCP which depends on the position of the ion in the BEC after time t . The color of the electrodes encodes, which field plates are used for applying the PFI and EF pulses shown in (a). (c) Distribution of the ion's time of flight t_{tof} as a function of evolution time t for $E = 4.3 \text{mV/cm}$ measured in a dense BEC (blue) and a low-density regime for reference (red). The low-density data is slightly offset in t for better visibility.

allows us to rapidly decelerate the produced ion and results in small initial velocities of $\lesssim 0.1 \text{m/s}$ (see Appendix A). In order to induce transport, the produced low-energy ionic impurity is now accelerated via a deliberately applied small electric field E of several mV/cm in magnitude pointing along the long y -axis of the BEC. After a variable evolution time t , we interrupt the transport dynamics with a two-step electric field pulse which rapidly extracts the ion from the BEC and guides it towards a microchannel plate (MCP) for detection [Fig. 2(a) and (b)]. The extraction sequence consists of a first field step to $E_{\text{ex},1} = 0.3 \text{V/cm}$ applied for $5 \mu\text{s}$, followed by a second step to $E_{\text{ex},2} = 54 \text{V/cm}$ for another $15 \mu\text{s}$. Since $E_{\text{ex},1}$ is too small to field-ionize the precursor Rydberg atom, this scheme allows us to distinguish the rare cases where ion creation was not successful by their time of flight to the detector and to

exclude them from the data analysis. Finally, the entire procedure is repeated 50 times with the same ensemble of atoms to gain statistics. Along its path to the MCP, the Rb^+ ion passes through an ion lens in einzel lens configuration, resulting in a time of flight t_{tof} to the detector which depends on the ion position prior to the extraction sequence [Fig. 2(b)]. In some cases, we detect a formed molecular ion Rb_2^+ , which due to its larger mass arrives at much later time at the MCP. The Rb_2^+ formation dynamics is investigated in section III.

Let us now focus on the distribution of the Rb^+ arrival times t_{tof} at the MCP. An exemplary data set for a field $E = 4.3 \text{ mV/cm}$ and different values of t is shown in Fig. 2(c) (blue bars). We compare this measurement to a reference data set taken at about 40 times smaller densities (red bars), for which the rate of ion-atom collisions ($\gamma_{\text{L}} \approx 24 \text{ kHz}$) is sufficiently small so that the ion motion is fully ballistic. Evidently, one finds that the ion arrives at systematically shorter times at the MCP when it is prepared in and accelerated through the dense BEC. This difference is a result of frequent ion-atom collisions, which we quantify in the following in more detail.

To this end, we study the transport dynamics of the ion through the BEC as a function of the applied electric field E . Representative measurements showing the distribution of the ion's time of flight t_{tof} to the MCP as a function of the transport time t are presented in Fig. 3(a) and (b) for two values of E . As before, the presence of ion-atom scattering causes systematic shifts of t_{tof} towards earlier times compared to reference measurements taken in a dilute collisionless regime of ballistic ion dynamics (red diamonds). For a quantitative analysis of this observation, we characterize our detection scheme through a detailed analysis of the ion's path to the MCP using a charged-particle trajectory solver (SIMION [28]). For our transport measurements in the BEC, this allows us to map the ion's mean time of flight (t_{tof}), depicted by the black circles, to its mean axial spatial coordinate ($\langle y_i \rangle$) in the BEC. Note that our analysis accounts for the specific electric-field and ion lens configuration of our setup and is carefully calibrated using the ballistic low-density reference data as described in more detail in Appendix B. The obtained mean ion position ($\langle y_i \rangle$) is indicated by the upper abscissa in Fig. 3.

Next, we compare our measurements to numerical simulations of the ionic transport dynamics through the condensate. To this end, the ion motion is modeled as a series of successive ion-atom collisions with ballistic motion in between [29, 30]. The time for a collision event to happen is Monte-Carlo sampled according to the ion-atom Langevin scattering rate γ_{L} . A second stochastically sampled parameter entering our simulation is the characteristic isotropic scattering angle (in the relative coordinate frame of the colliding ion-atom pair) of spiraling-type Langevin collisions. This stochastic trajectory approach allows us to account for the varying atomic density which the ion probes on its path through the trapped condensate, as well as for the spatial distribution of initial ion positions characterized by the Gaussian profile of our Rydberg excitation laser. Note that for the moment, we assume only elastic collisions and also neglect the much lower temperature of the atoms in the BEC as compared to the average ion

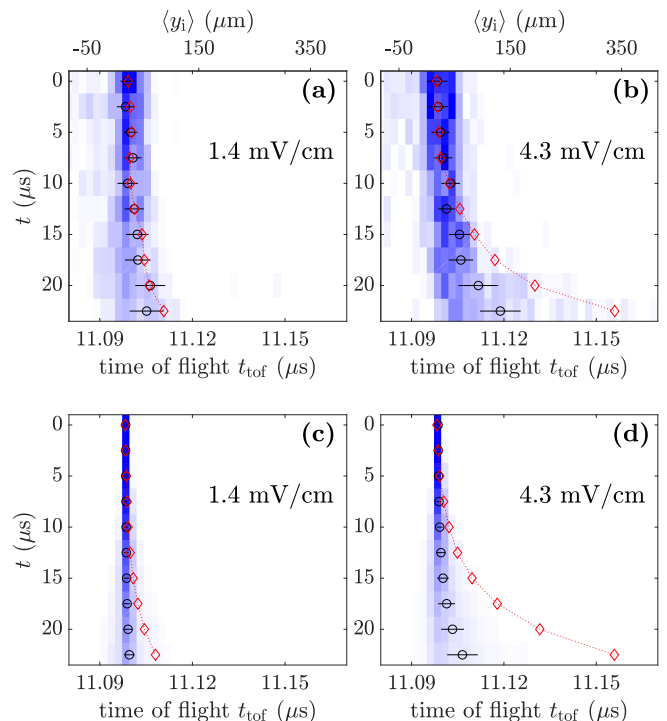


FIG. 3. Ion transport through the BEC for an electric field $E = 1.4 \text{ mV/cm}$ (a,c) and $E = 4.3 \text{ mV/cm}$ (b,d). Shown are the measured (top row) and numerically simulated (bottom row) distributions of the ion's time of flight to the MCP as a function of transport time t . The color scale encodes the normalized ion signal as shown in Fig. 2(c). Black circles depict means of the measured and simulated time of flight distributions (t_{tof}) and the horizontal bars indicate the corresponding widths at half maximum. For comparison, the red diamonds are measurements and simulations, respectively, of (t_{tof}) for a ballistic ion dynamics at low density. The upper abscissa in (a) and (b) indicates the mapped mean ion position ($\langle y_i \rangle$) (see text).

kinetic energy. We have also verified that glancing-type forward scattering collisions, which are not accounted for by the Langevin rate, do not significantly affect the transport dynamics. Details of the model are described in Appendix D. Numerical results of this model, after a subsequent propagation through our ion-detection setup as described above, deliver the full time-dependent distribution of t_{tof} . A comparison of the simulated data for the two explored electric field values [Fig. 3(c) and (d)] with the experiment yields good agreement, despite a small systematic mismatch that points to a slightly higher mobility of the ion in the experiment (see also below for a more detailed discussion).

Our analysis shows that the reported experiment explores a regime of frequent ion-atom collisions, as a result of which the ionic impurity quickly reaches a state of diffusive transport. This diffusive transport is characterized by a constant drift motion with an electric-field-dependent mean velocity ($\langle v_i \rangle_{\text{d}}$ [cf. Fig. 1(b)]. To extract a drift velocity from our measurements, we evaluate the time evolution of the mean ion position ($\langle y_i \rangle$) from data sets as shown in Fig. 3. Results for four different values of E are shown in Fig. 4(a) together with linear fits to the data, the slopes of which yield values for $\langle v_i \rangle_{\text{d}}$.

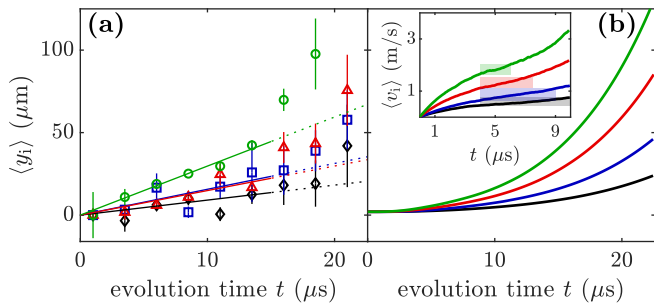


FIG. 4. (a) Mean position $\langle y_i \rangle$ of the ion accelerated through the BEC as a function of evolution time t for $E = 1.4$ (black diamonds), 2.8 (blue squares), 4.3 (red triangles), 5.7 (green circles) mV/cm. Error bars originate from the standard deviation of the fitted center of the ion time of flight distribution to its center of mass. Solid lines show linear fits to the data for $t < 15 \mu\text{s}$ to analyze the ion's diffusive motion and to extract the associated drift velocity $\langle v_i \rangle_d$. (b) Numerically simulated mean ion position $\langle y_i \rangle$ as a function of evolution time t for the same values of E as in (a), depicted in the same color. The inset shows the corresponding mean particle velocity $\langle v_i \rangle$. The shaded regions indicate the characteristic plateau of nearly constant transient drift velocity.

Note that for the case of our finite size condensate, the diffusive motion is a transient state which turns over into ballistic dynamics once the ion approaches the edge of the condensate. For this reason and guided by our numerical calculations, the linear fits for extracting $\langle v_i \rangle_d$ exclude data points for $t > 15 \mu\text{s}$. The transient character of the diffusive transport is also apparent in the corresponding simulated time evolution of $\langle v_i \rangle$ and $\langle y_i \rangle$ shown in Fig. 4(b), which, as mentioned above, takes into account the BEC shape as well as the distribution of the initial ion position.

The electric field dependence of $\langle v_i \rangle_d$ obtained from the linear fits in Fig. 4(a) is shown in Fig. 5 (blue diamonds). The data follow a clear linear dependence from which we deduce a mobility for the ionic impurity in our BEC $\mu_{\text{ion}}^{\text{exp}} = \partial \langle v_i \rangle_d / \partial E = (47 \pm 16) \times 10^3 \text{ cm}^2/(\text{Vs})$. Finally, the measurements are compared to the prediction from the stochastic trajectory simulation (black triangles), which yields $\mu_{\text{ion}}^{\text{sim}} = (33 \pm 3) \times 10^3 \text{ cm}^2/(\text{Vs})$. The numerical results in Fig. 5 are obtained from linear fits to the simulated data for $\langle y_i \rangle$ for the same range of t as for the experimental data points, and coincide within $\lesssim 7\%$ with drift velocities obtained from the transient plateau in $\langle v_i \rangle_d$ [cf. inset to Fig. 4(b)]. We notice that the measured ion mobility is slightly larger than the numerical model prediction. This deviation may be attributed to formation of weakly bound molecular ions. Although we exclude events leading to molecule formation from the transport analysis as mentioned above, this competing mechanism, however, should alter the effective initial ion distribution in our creation volume. More specifically, molecular ion formation depends sensitively on the local density and is expected to appear more often in the central and densest region of the creation volume. Consequently, our numerical analysis likely overestimates the contribution of ions to the transport dynamics which start their trajectory at the very center of the BEC.

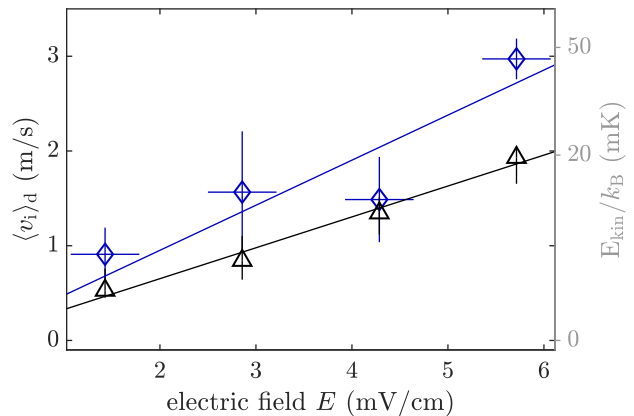


FIG. 5. Drift velocity and mobility of the ion in the BEC. Measured (blue diamonds) and simulated (black triangles) drift velocity $\langle v_i \rangle_d$ as a function of the applied electric field E . For the measurement data, vertical and horizontal error bars result from the uncertainty of the linear fits in Fig. 4(a) and indicate the level of stray field control ($\pm 300 \mu\text{V/cm}$) in our setup, respectively. Error bars for the numerical data reflect the shaded regions around $\langle v_i \rangle_d$ in the inset of Fig. 4(b). Solid lines are linear fits to the data to extract the ion mobility (see text). The right ordinate shows the kinetic energy of the ion corresponding to $\langle v_i \rangle_d$.

Evidently, such an effect systematically reduces the effective atomic density and qualitatively leads to a larger ion mobility. By excluding the central 30% of the ions from our numerical simulations, we estimate that such an effect may alter $\mu_{\text{ion}}^{\text{sim}}$ by about 10%. An experimental analysis of the fraction of molecular ions formed during the transport is provided in Appendix C. In the next section, we focus in detail on the associated inelastic collision dynamics and the underlying ultracold chemistry observed in our BEC.

III. THREE-BODY RECOMBINATION AND MOLECULAR-ION ROVIBRATIONAL QUENCHING

For the measurements of ionic transport through the BEC, we have analyzed the time of flight distribution of Rb^+ on the MCP. In a fraction of the experimental realizations, however, we detect a Rb_2^+ molecular ion instead, which we can discriminate in our apparatus by time of flight mass spectrometry (see Appendix C). In contrast to the elastic Rb^+ scattering studied above, the Rb_2^+ molecular ions we detect here are a result of inelastic two- and three-body collisions. In the following, we will focus on their formation kinetics in the condensate. To this end, we apply the same measurement sequence as in the previous section, but now null the applied electric field E during the evolution time t down to our level of stray field control (i.e. $E \lesssim 300 \mu\text{V/cm}$ in all three spatial directions). The mean Rb^+ and Rb_2^+ ion counts detected on the MCP as a function of t , shown in Fig. 6(a), provide direct evidence for the formation of molecular ions on a timescale of about $10 \mu\text{s}$. Note that the sum of the two signals (triangles) remains constant over the measurement time. Consequently, for each lost Rb^+

we observe that a Rb_2^+ molecular ion is formed.

Starting from a single low-energy ion immersed in the condensate, Rb_2^+ can only result from a reactive Rb-Rb-Rb^+ three-body recombination collision. Three-body recombination in charge-neutral hybrid systems has been observed for trapped Rb^+ and also Ba^+ , comprising studies of the energy scaling of the recombination rate coefficient K_3 [16, 31]. In contrast, our experimental approach provides unique means to explore the reaction products in more detail and moreover measure their subsequent dynamics, complementing very recent observation of intriguing light-assisted reaction kinetics of BaRb^+ [32]. Specifically, we exploit the previously described extraction sequence, labeled EF in Fig. 2(a), to dissociate the produced molecular ion with the electric field $E_{\text{ex},2}$. Assume the molecular ion is in a certain weakly-bound rovibrational state prior to the electric field pulse $E_{\text{ex},2}$. It will then only be detected in the Rb_2^+ channel at the MCP when $E_{\text{ex},2}$ is smaller than the field dissociation threshold of this state. Otherwise the molecule is dissociated and the resulting fragment Rb^+ is detected. Consequently, the fraction η of detected Rb_2^+ as a function of $E_{\text{ex},2}$ measures the total population of molecular states which are deeper bound than the critical binding energy E_b^{crit} associated with $E_{\text{ex},2}$.

Measurements of η versus $E_{\text{ex},2}$ are shown in Fig. 6(b) for two different values of the evolution time t . First, for $t = 6 \mu\text{s}$ we notice a clear increase in η at small values of $E_{\text{ex},2}$, which points at a tendency that three-body recombination likely produces very weakly-bound states. Second, the data set for longer evolution time shows an overall increase in η but also indicates redistribution into more deeply-bound states. In a next step, we aim to identify $E_{\text{ex},2}$ more quantitatively with E_b^{crit} . To first approximation, one may relate $E_{\text{ex},2}$ with E_b^{crit} using a simple one-dimensional classical barrier model for the dissociation (Appendix E). In the experiment, however, this mapping is expected to be systematically altered due to random molecular alignment, molecular rotation, and the finite ramp time of the electric field. We therefore relate $E_{\text{ex},2}$ with E_b^{crit} via more detailed classical simulations of the dissociation dynamics where we account for fully randomized molecular alignment and adiabatic state changes upon dissociation. This yields the dependance of η on E_b^{crit} shown in Fig. 6(c).

Consequently, this approach delivers values for E_b^{crit} which only include vibrational dynamics. We have checked that adding rotational dynamics to the dissociation model yielding E_b^{crit} does not qualitatively change the trend of the data. The data in Fig. 6(c) may thus now be compared to a Langevin capture model describing pure vibrational relaxation dynamics, as recently introduced in [33]. Our modeling of the experimental results incorporates two processes. The first one is the formation of weakly-bound molecular ions by three-body recombination. This is followed by secondary two-body collisions of the produced molecule with atoms from the BEC, which result in vibrational relaxation into more deeply bound states [cf. Fig. 1(c)]. Indeed, the importance of vibrational quenching collisions for our experiment can already be seen from a simple estimate. As for the atomic ion-atom scattering discussed above, collisions of Rb_2^+ with a neutral Rb atom are induced by the same long-range C_4 potential, giv-

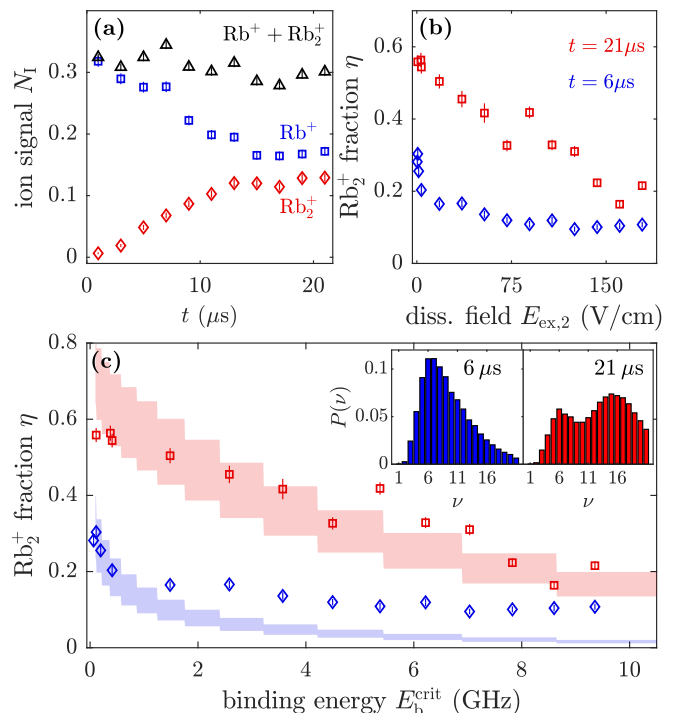


FIG. 6. Three-body recombination and molecular-ion rovibrational quenching. (a) Rb^+ (blue squares) and Rb_2^+ (red diamonds) signal as a function of evolution time t measured for zero bias electric field E and with the Rb_2^+ dissociation field set to $E_{\text{ex},2} = 89 \text{ V/cm}$. Black triangles show the sum of the Rb^+ and Rb_2^+ signal. (b) Fraction η of detected Rb_2^+ as a function of the dissociation electric field $E_{\text{ex},2}$ (c) η as a function of the critical molecular binding energy E_b^{crit} , which is the threshold value beyond which molecules are dissociated in the electric field $E_{\text{ex},2}$ (see text). Data sets are for $t = 6 \mu\text{s}$ (diamonds) and $t = 21 \mu\text{s}$ (squares). Insets: Distribution $P(\nu)$ of the most weakly-bound states for $t = 6$ and $21 \mu\text{s}$ obtained from the numerical simulations.

ing comparable rates for spiraling-type Langevin collisions $\gamma_{\text{L}}^{\text{mol}} = 2\pi n_{\text{at}} \sqrt{C_4/\mu_{\text{mol}}}$, where μ_{mol} is now the reduced mass of the molecule-atom system [33]. The molecule-atom system, however, features additional coupling of molecular states at short range, which inevitably results in inelastic vibrational relaxation for each Langevin collision. The large collision rate $\gamma_{\text{L}}^{\text{mol}}$ in our dense gas can then easily yield multiple of such secondary collision events before the molecular ion exits the condensate, even for the considerable kinetic energy release associated with the Rb_2^+ formation.

We model our experimental results in an analog way as in the previous section using a stochastic trajectory approach, but now incorporating the two inelastic processes discussed above. In brief, we start out with a first three-body recombination collision at a time sampled according to the recombination rate coefficient K_3 . Subsequently, the product molecular ion undergoes further quenching collisions at random times determined by the Langevin rate $\gamma_{\text{L}}^{\text{mol}}$. After each collision the molecule's velocity is increased by the associated kinetic energy release. Similar to our modeling of the transport dy-

namics, we keep track of the free motion of the molecular ion between successive collisions, which allows us to account for the density distribution of the condensate. An integral input to this simulation is a computed distribution of product molecular states for the first three-body recombination event as well as branching ratios for the subsequent vibrational relaxation processes. The former depends on the typical ion kinetic energy E_{kin}^{3b} in our system prior to the recombination [31]. The computation of the vibrational branching is based on the distorted wave Born approximation as described in Ref. [33]. For a more detailed description of the model see Appendix D. Results of these simulations are shown in Fig. 6(c) as shaded regions. We find good agreement with the experimental observation on a qualitative level, and even quantitatively the numerical results seem to only slightly underestimate the fraction of more deeply-bound molecular states for the data set taken at $t = 6 \mu\text{s}$. Note that the only free parameters entering our model are the value for K_3 and the initial kinetic energy of the ion E_{kin}^{3b} , which influences the distribution of the recombination products. Specifically, the results in Fig. 6(c) are obtained for $K_3 = 6(2) \times 10^{-25} \text{ cm}^6/\text{s}$ and $E_{\text{kin}}^{3b} = k_B \times 5(2) \text{ mK}$, where the numbers in parentheses reflect the width of the shaded regions. The recombination rate coefficient we obtain here is in fairly good agreement with previous observations using trapped Rb^+ [16], and the value for E_{kin}^{3b} can be understood from residual stray electric fields accelerating the ion prior to the three-body reaction.

Interestingly, our numerical approach delivers the recombination and subsequent vibrational quenching dynamics on the level of individual molecular states. The insets in Fig. 6(c) show the obtained distribution $P(v)$ of the most weakly-bound vibrational states v [34], to which our measurement is particularly sensitive, for the two experimentally investigated evolution times and for the values of K_3 and E_{kin}^{3b} given above. In the very early stage of the dynamics $P(v)$ reflects the product distribution of the three-body recombination. At later times, the dynamics reveals the two-body vibrational quenching marked by the transfer of population to more deeply-bound molecular states.

IV. CONCLUSION AND OUTLOOK

In conclusion, we have investigated transport of a single low-energy ionic impurity through a Bose-Einstein condensate in the absence of an ion trap but rather controlled by an electrically well shielded environment. The charged impurity is produced from a single Rydberg atom via a double-pulse field-ionization scheme which minimizes its initial kinetic energy. This approach allowed us to steer the ion through the condensate via small electric bias fields, to observe indications of diffusive transport, and to measure the ion's mobility. Our observations are possible due to the comparatively high BEC density in combination with the large ion-atom Langevin scattering cross section, which causes frequent collisions on a tens of microseconds timescale before the ion exits the gas.

While the transport dynamics studied in this work is well explained by semi-classical Langevin collisions, the reported

approach can be advanced in future experiments to access even lower collision energies, possibly reaching a regime where only few partial waves contribute to the scattering process and quantum effects start to dictate the transport. This requires improved stray field control and better spatial resolution, specifically for the early stage of the dynamics during which the ion kinetic energy is particularly small. To this end, it is very appealing to augment the techniques presented here by ion-imaging optics, which is currently explored for ultracold Rydberg experiments, and which allows for sub-micrometer spatial resolution [35]. This provides exciting prospects to study spatially resolved ultracold ion-atom scattering down to the level of individual collisions [36], comprising quantum effects for ion impurity transport and associated polaron-type dynamics [21, 37].

Furthermore, we have demonstrated means to distinguish inelastic collision processes producing weakly-bound molecular ions from elastic transport dynamics. Evidently, this is a valuable feature also for future experiments with ions in the dense regime of quantum degenerate gases, and may prove beneficial for studies of predicted ionic many-body complexes at lower temperatures [19, 20]. Finally, it seems appealing to elaborate strategies to boost the sensitivity of our field-dissociation probe of the produced weakly-bound molecular ions, ideally to a level of resolved quantum states [38], e.g. by exploiting additional microwave spectroscopy [39].

ACKNOWLEDGMENTS

We acknowledge support from Deutsche Forschungsgemeinschaft [Projects No. PF 381/13-1 and No. PF 381/17-1, the latter being part of the SPP 1929 (GiRyd)] and the Carl Zeiss Foundation via IQST. F. M. is indebted to the Baden-Württemberg-Stiftung for the financial support by the Eliteprogramm for Postdocs.

APPENDIX

A. Pulsed field ionization characterization

Here, we characterize the performance of the pulsed field ionization (PFI) sequence used to produce the low-energy ionic impurity and explained in section II of the main text. The following data are all obtained in a dilute thermal cloud with $n_{\text{at}} \approx 1 \times 10^{13} \text{ cm}^{-3}$ to exclude any collision effects. First, the ionization efficiency of the precursor $160S_{1/2}$ Rydberg atom by the first 10 ns long ionization pulse is analyzed. In this measurement, we do not yet apply a second field pulse of opposite polarity. Fig. 7 shows the signal of produced Rb^+ (blue diamonds) and detected Rydberg atoms (red squares) as a function of the height of the field ionization pulse. We find that the $160S_{1/2}$ Rydberg level is ionized between 0.7 and 2V/cm with an overall efficiency of $> 90\%$ for $E \geq 2 \text{ V/cm}$. Instrumental for this analysis is the applied two-step electric field detection sequence (labeled EF in Fig. 2(a)),

which allows us to temporally distinguish Rb^+ ions and Rydberg atoms on the MCP [Fig. 7(b)]. Note that the latter are ionized by the field $E_{\text{ex},2}$ of the detection sequence.

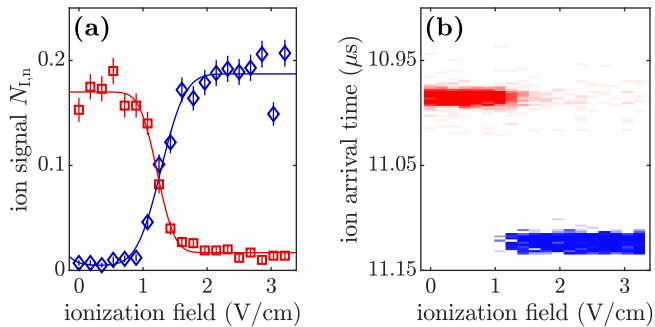


FIG. 7. Pulsed field ionization (PFI) to produce a single ionic impurity. (a) Rb^+ ion (blue diamonds) and $160\text{S}_{1/2}$ Rydberg atom (red squares) signal resulting from the 10 ns long PFI as function of the height of the field ionization pulse. Solid lines are error-function fits to the data to guide the eye. (b) Temporal separation of ion and Rydberg atom signal on the MCP. Ions produced by the PFI arrive at $11.12 \mu\text{s}$, whereas Rydberg atoms (ionized by $E_{\text{ex},2}$) arrive at $10.98 \mu\text{s}$.

Next, we add the second short electric field pulse of opposite polarity to the PFI sequence, which aims to minimize the Rb^+ velocity and thus produces a cold low-energy impurity. To quantify the performance of this stopping procedure, we let the ion evolve for $t = 21 \mu\text{s}$ in a bias electric field set to $E = 4.3 \text{ mV/cm}$ and monitor its time of flight t_{tof} to the MCP as a function of the nominal height of the second stop pulse (squares in Fig. 8). The change in t_{tof} already indicates the influence of the stop pulse. Specifically, smaller values of t_{tof} correspond to ion positions closer to the initial point of creation. However, this observation does not yet allow to identify the value of the second pulse height which leads to a minimal initial velocity. Therefore, we repeat the measurement but with the polarity of the two pulses reversed (diamonds in Fig. 8). This inverts the observed slope. The crossing point indicates a setting where the PFI sequence causes minimal velocity of the produced ion and thus allows for deducing the optimal value of the stop pulse height. For the experiments presented in the main text, the stop pulse height is thus chosen to -2.66 V/cm . Moreover, a comparison of the data with our SIMION simulation allows us to quantify the ion's initial velocity to $\lesssim 0.1 \text{ m/s}$ (shaded region in Fig. 8). Note that the initial velocity of the ion in the absence of the stop pulse can be estimated in the same way to $\pm 2 \text{ m/s}$ depending on the polarity of the first field pulse (dotted lines in Fig. 8).

B. SIMION simulations

The quantitative analysis of the diffusive transport of the ion in the BEC involves simulations of our ion detection sequence using the charged-particle trajectory solver SIMION [28]. These simulations require a careful calibration taking into account the specific electric field and ion-lens configura-

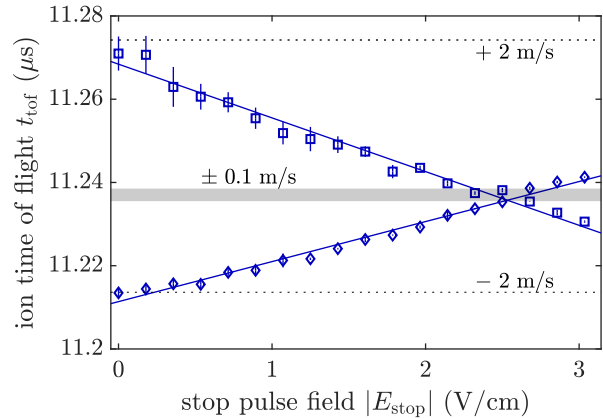


FIG. 8. Characterization of the stopping procedure for minimizing the initial ion velocity. Mean time of flight t_{tof} of the ion to the MCP for $t = 21 \mu\text{s}$ and $E = 4.3 \text{ mV/cm}$ as a function of the nominal height of the stop pulse. Squares (diamonds) show data for which the first pulse (2.85 V/cm) of the PFI double-pulse sequence is aligned (anti-aligned) with the bias field E . Error bars for the experimental data originate from the standard deviation of the fitted center of the ion time of flight distribution to its center of mass. The shaded region and dotted lines indicate predicted values of t_{tof} for ions with initial velocity $\lesssim 0.1 \text{ m/s}$ and $\pm 2 \text{ m/s}$, respectively, as obtained from SIMION simulations. Solid lines are linear fits to the data and indicate the crossing point giving the optimal stop pulse field.

tion in our setup. First, the high voltage (-2.35 kV) applied to the front plate of the MCP as well as to the last cylinder of the einzel lens leads to stray electric fields in the BEC region. Like in the experiment, such stray fields need to be compensated. In the simulation, we minimize these fields at the initial ion position by applying differential voltages to opposing field plates. Second, we use the low-density experimental data, i.e. the ballistic ion motion, for a fine calibration of the SIMION simulations. We find that we need to introduce two calibration parameters in order to reproduce the ion's time of flight distribution as a function of the evolution time t . Those are a gradient in the electric field and a small shift of the initial ion position with respect to the electrode center both along the y -axis (long axis of the BEC). The calibration procedure yields optimal agreement with the ballistic experimental data for a shift of $50 \mu\text{m}$ and a field gradient of 1.18 mV/cm across $10 \mu\text{m}$. The field gradient is most likely a result of surface charges on the vacuum glass cell of our setup. Note that we have independently verified the presence and also the magnitude of the field gradient via Stark spectroscopy measurements for several positions of the Rydberg excitation along the y -axis.

C. Rb^+ and Rb_2^+ signal on the MCP

A central aspect of our experimental approach is the capability to distinguish diffusive transport of Rb^+ in the BEC from the competing mechanism of ion-atom-atom three-body recombination resulting in the formation of weakly bound

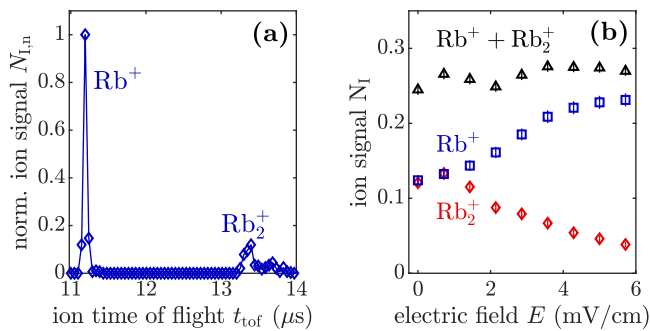


FIG. 9. (a) Time of flight distribution of ion counts on the MCP for an electric field $E = 4.8$ mV/cm and $t = 21$ μ s. Rb^+ ions arrive around 11.2 μ s whereas Rb_2^+ molecular ions arrive around 13.4 μ s. (b) Rb^+ (blue squares) and Rb_2^+ (red diamonds) signal as a function of the transport electric field E after an evolution time $t = 21$ μ s. Black triangles show the sum of the Rb^+ and Rb_2^+ signal. In (a) and (b), the Rb_2^+ dissociation field is set to $E_{\text{ex},2} = 54$ V/cm.

Rb_2^+ . This is accomplished by time of flight mass spectrometry as demonstrated in Fig. 9(a), which shows the time of flight distribution at the MCP over a wider range of values as compared to Figs. 2 and 3 of the main text. Due to their larger mass and thus longer t_{tof} to reach the detector, Rb_2^+ molecular ions can be well separated from the Rb^+ channel. For the ion transport analysis, we can thus solely focus on the dynamics of the time of flight distribution in the Rb^+ channel and exclude realizations which result in molecule formation.

While the Rb_2^+ formation dynamics in section III is investigated in zero electric bias field, here, we present supplemental data showing the fraction of ions which undergo a chemical reaction during the transport as a function of the transport electric field E after an evolution time of $t = 21$ μ s (see Fig. 9(b)). For the smallest electric field studied in this work, almost $\approx 42\%$ of the initially generated ions undergo a chemical reaction after $t = 21$ μ s. With increasing transport field this effect becomes less prominent, leading to a molecular fraction of $\approx 14\%$ for the largest transport electric field of 5.7 mV/cm investigated.

D. Stochastic trajectory simulations

The numerical simulations of the ion transport reported in the main text are based on Monte-Carlo sampled classical trajectories sequentially interrupted by ion-atom Langevin collisions, a model which was first developed to model buffer-gas cooling dynamics of a trapped ion [29]. Specifically, a single ion trajectory of the Monte-Carlo sample is computed assuming that the ion starts from its initial position \mathbf{x}_i^0 and follows a classical trajectory in the applied electric field E . After a randomly sampled time t_n , a collision happens which changes the ion's current velocity \mathbf{v}_i^n instantaneously to a new value \mathbf{v}_i^{n+1} . The elastic nature of the collision implies that, in the relative coordinate frame of a colliding ion-atom pair, the updated relative velocity $\mathbf{v}_{\text{rel}}^{n+1} = R(\theta^n, \phi^n)\mathbf{v}_{\text{rel}}^n$ [30]. Here, R is a rotation matrix with polar angles θ^n and ϕ^n . Accord-

ingly, in the laboratory frame the ion velocity after the collision reads $\mathbf{v}_i^{n+1} = 1/2[\mathbf{v}_i^n + R(\theta, \phi)\mathbf{v}_i^n]$, where we have assumed that the colliding neutral atom is initially at rest, which is justified by the small BEC temperature compared to the kinetic energy of the ion. The relative collision angles θ^n and ϕ^n entering the rotation matrix are to be sampled according to the ion-atom differential cross section. For the spiraling-type Langevin collisions relevant for this work, θ^n and ϕ^n are drawn uniformly on the unit sphere, i.e. resembling the hard-sphere Langevin differential scattering cross section. Finally, the time steps t_n between successive collisions are randomly sampled according to the energy-independent but density-dependent Langevin scattering rate $\chi_L = 2\pi n_{\text{at}}\sqrt{C_4}/\mu$ [27]. This allows us to account for the Thomas-Fermi density profile $n_{\text{at}}(x, y, z)$ of the BEC with parameters given in the main text. Note that we also take care of the fact that n_{at} changes during the motion of the ion between collisions by applying the sampling algorithm for t^n described in Ref. [29].

Finally, the results in the main text are obtained by typically 500 such trajectories. For the numerical data shown in Fig. 1(b), the ion's initial position for each trajectory is the BEC center. For the numerical results which are compared to the experimental data in Fig. 3, Fig.4(b), and Fig. 5, the ion's initial position is randomly sampled according to the Gaussian profile of our Rydberg excitation laser and the BEC density profile. These data sets also include averaging over small stray electric fields of ± 1 mV/cm in all three directions. Incorporating these stray fields has practically no influence on the mobility simulations, but slightly broaden the distributions shown in Fig. 3.

Note that this treatment ignores the glancing-type collisions with small scattering angles. Indeed, these collisions barely affect the motion of the ion and do not contribute to diffusion or thermalization processes [27], but it is a priori not clear that they do not affect the transport dynamics in our finite size sample. For this reason, we have performed additional simulations where the scattering angles are sampled according to the full quantum mechanical ion-atom elastic scattering cross section derived from a random-phase approximation [29]. This elastic cross section features a pronounced forward scattering peak, indicative of the glancing collisions. Here, the time steps t_n are sampled according to the total elastic cross section $\sigma_{\text{el}} = \pi(\mu C_4^2)^{1/3}(1 + \pi^2/16)E_c^{-1/3}$, which accounts for the additional frequent glancing collisions (E_c is the collision energy) [27]. Comparing the two approaches, we find no discernible difference and thus conclude that glancing collisions are not relevant for the dynamics we observe in our experiments.

To simulate the dynamics of the Rb_2^+ molecular ion, we also employ classical trajectories through the BEC in an analogue way as described above, but now consider vibrationally inelastic processes. At first, these simulations need the initial state of the molecule as an input. In order to obtain a reasonable estimate for the latter, we assume that the three-body collision process leading to molecule formation is sequential, meaning that one atom quenches the two-body ion-atom scattering state, resulting in occupation of multiple bound states with probabilities proportional to the wave function overlaps.

This results in a broad distribution of initially occupied bound states with the maximum corresponding to the initial kinetic energy E_{kin}^{3b} of the ion-atom pair. Note that the more deeply bound states have higher initial velocity due to larger energy release. The instant of the three-body recombination event is randomly sampled from an exponential decay determined by the associated recombination rate coefficient K_3 .

The subsequent inelastic vibrational quenching collisions enter the stochastic trajectory model as a reactive process happening with the Langevin rate $\gamma_{\text{L}}^{\text{mol}}$ and leading to a change in the internal state and an increase of the kinetic energy of the molecule. The distribution of product states for such a process is calculated by means of the distorted wave Born approximation [33]. In brief, the state-to-state transition probability is proportional to the square of the inelastic elements of the K matrix, which can be approximated as $K_{if} \propto \int dR \phi_i(R) \phi_f(R) V_{if}(R)$ with V_{if} being the coupling potential between the channels. Finally, as the Langevin differential cross section is largely isotropic, we can draw the deflection angles for the rotation matrix R again from the unit sphere. The numerical data in Fig. 6(b) and (c) are obtained from typically 10^5 trajectories.

E. Dissociation field and critical binding energy

In Fig. 6(b) of the main text, we show the measured fraction η of detected Rb_2^+ molecular ions as a function of the dissociation field $E_{\text{ex},2}$. The latter is then associated with a critical minimum binding energy $E_{\text{b}}^{\text{crit}}$ that a molecule needs to have in order to withstand dissociation by the field $E_{\text{ex},2}$ and thus to contribute to η . To relate $E_{\text{b}}^{\text{crit}}$ with $E_{\text{ex},2}$, we first consider a simple over-the-barrier model for the dissociation. To this

end, we start with the long-range tail of the molecular ion potential in the presence of the external field $E_{\text{ex},2}$ (q denotes the elementary charge)

$$V_{\text{tot}}(R) = -\frac{C_4}{2 \cdot R^4} - \frac{1}{2} \cdot q \cdot E_{\text{ex},2} \cdot R, \quad (1)$$

which exhibits a field-dependent saddle point. Dissociation occurs now for all molecular states with binding energy smaller than the height of this potential barrier induced by $E_{\text{ex},2}$. Consequently, one finds for the critical binding energy

$$E_{\text{b}}^{\text{crit}} = -\frac{C_4}{2} \left(4 \cdot \frac{C_4}{qE_{\text{ex},2}} \right)^{-\frac{4}{3}} - \frac{qE_{\text{ex},2}}{2} \left(4 \cdot \frac{C_4}{qE_{\text{ex},2}} \right)^{\frac{1}{3}}. \quad (2)$$

This simple one-dimensional picture, however, only holds for a molecular ion with an internuclear axis aligned along the electric field. In the experiment, however, we expect the mapping to be altered due to random molecular alignment and molecular rotation. Furthermore, this model assumes a diabatic quench of the initial rovibrational state into a situation where the electric field is instantly present. In the experiment, however, the dissociation field is ramped up within a finite time of typically ≈ 20 ns. We therefore extend our model by performing classical trajectory simulations of the dissociation dynamics. We now take into account random molecular orientation of the molecule in the laboratory frame and adiabatic state changes upon dissociation. From these simulations, we find a modified relation between $E_{\text{ex},2}$ and $E_{\text{b}}^{\text{crit}}$, which follows the functional dependence of Eq. 2 but with an effective value $C_4^{\text{eff}} = 10.48$ a.u. obtained by fitting Eq. 2 to the numerical results. This modified relation yields the red squares and blue diamonds in Fig. 6(c).

-
- [1] C.-C. Chien, S. Peotta, and M. Di Ventura, *Nat. Phys.* **11**, 998 (2015).
- [2] S. Krinner, D. Stadler, D. Husmann, J.-P. Brantut, and T. Esslinger, *Nature* **517**, 64 (2015).
- [3] A. Schirotzek, C.-H. Wu, A. Sommer, and M. W. Zwierlein, *Phys. Rev. Lett.* **102**, 230402 (2009).
- [4] C. Kohstall, M. Zaccanti, M. Jag, A. Trenkwalder, P. Massignan, G. M. Bruun, F. Schreck, and R. Grimm, *Nature* **485**, 615 (2012).
- [5] M. Koschorreck, D. Pertot, E. Vogt, B. Fröhlich, M. Feld, and M. Köhl, *Nature* **485**, 619 (2012).
- [6] N. B. Jørgensen, L. Wacker, K. T. Skalmstang, M. M. Parish, J. Levins, R. S. Christensen, G. M. Bruun, and J. J. Arlt, *Phys. Rev. Lett.* **117**, 055302 (2016).
- [7] M. Hohmann, F. Kindermann, T. Lausch, D. Mayer, F. Schmidt, E. Lutz, and A. Widera, *Phys. Rev. Lett.* **118**, 263401 (2017).
- [8] S. Palzer, C. Zipkes, C. Sias, and M. Köhl, *Phys. Rev. Lett.* **103**, 150601 (2009).
- [9] F. Meinert, M. Knap, E. Kirilov, K. Jag-Lauber, M. B. Zvonarev, E. Demler, and H.-C. Nägerl, *Science* **356**, 945 (2017).
- [10] M. Tomza, K. Jachymski, R. Gerritsma, A. Negretti, T. Calarco, Z. Idziaszek, and P. S. Julienne, *Rev. Mod. Phys.* **91**, 035001 (2019).
- [11] C. Zipkes, S. Palzer, C. Sias, and M. Köhl, *Nature* **464**, 388 (2010).
- [12] Z. Meir, T. Sikorsky, R. Ben-shlomi, N. Akerman, Y. Dallal, and R. Ozeri, *Phys. Rev. Lett.* **117**, 243401 (2016).
- [13] T. Feldker, H. Fürst, H. Hirzler, N. V. Ewald, M. Mazzanti, D. Wiater, M. Tomza, and R. Gerritsma, *Nat. Phys.* (2020). <https://doi.org/10.1038/s41567-019-0772-5>
- [14] J. Schmidt, P. Weckesser, F. Thielemann, T. Schaetz, and L. Karpa, *Phys. Rev. Lett.* **124**, 053402 (2020).
- [15] A. T. Grier, M. Cetina, F. Oručević, and V. Vuletić, *Phys. Rev. Lett.* **102**, 223201 (2009).
- [16] A. Härter, A. Krüchow, A. Brunner, W. Schnitzler, S. Schmid, and J. Hecker Denschlag, *Phys. Rev. Lett.* **109**, 123201 (2012).
- [17] L. Ratschbacher, C. Zipkes, C. Sias, and M. Köhl, *Nat. Phys.* **8**, 649 (2012).
- [18] T. Sikorsky, Z. Meir, R. Ben-shlomi, N. Akerman, and R. Ozeri, *Nat. Commun.* **9**, 920 (2018).
- [19] R. Côté, V. Kharchenko, and M. D. Lukin, *Phys. Rev. Lett.* **89**, 093001 (2002).
- [20] J. M. Schurer, A. Negretti, and P. Schmelcher, *Phys. Rev. Lett.* **119**, 063001 (2017).
- [21] R. Côté, *Phys. Rev. Lett.* **85**, 5316 (2000).

- [22] F. Reif and L. Meyer, *Phys. Rev.* **119**, 1164 (1960).
- [23] G. W. Rayfield and F. Reif, *Phys. Rev. Lett.* **11**, 305 (1963).
- [24] J. B. Balewski, A. T. Krupp, A. Gaj, D. Peter, H. P. Büchler, R. Löw, S. Hofferberth, and T. Pfau, *Nature* **502**, 664 (2013).
- [25] F. Engel, T. Dieterle, T. Schmid, C. Tomschitz, C. Veit, N. Zuber, R. Löw, T. Pfau, and F. Meinert, *Phys. Rev. Lett.* **121**, 193401 (2018).
- [26] W. F. Holmgren, M. C. Revelle, V. P. A. Lonij, and A. D. Cronin, *Phys. Rev. A* **81**, 053607 (2010).
- [27] R. Côté and A. Dalgarno, *Phys. Rev. A* **62**, 012709 (2000).
- [28] SIMION v.8.1.1., Scientific Instrument Services (SIS).
- [29] C. Zipkes, L. Ratschbacher, C. Sias, and M. Köhl, *New J. Phys.* **13**, 053020 (2011).
- [30] K. Chen, S. T. Sullivan, and E. R. Hudson, *Phys. Rev. Lett.* **112**, 143009 (2014).
- [31] A. Krüchow, A. Mohammadi, A. Härter, J. Hecker Denschlag, J. Pérez-Ríos, and C. H. Greene, *Phys. Rev. Lett.* **116**, 193201 (2016).
- [32] A. Mohammadi, A. Krüchow, A. Mahdian, M. Deiß, J. Pérez-Ríos, H. da Silva Jr., M. Raoult, O. Dulieu, and J. Hecker Denschlag, arXiv:2005.09338 (2020).
- [33] K. Jachymski and F. Meinert, *Appl. Sci.* **10**, 2371 (2020).
- [34] We count the quantum number ν of the vibrational states of Rb_2^+ starting from the dissociation threshold.
- [35] M. Stecker, H. Schefzyk, J. Fortágh, and A. Günther, *New J. Phys.* **19**, 043020 (2017).
- [36] T. Schmid, C. Veit, N. Zuber, R. Löw, T. Pfau, M. Tarana, and M. Tomza, *Phys. Rev. Lett.* **120**, 153401 (2018).
- [37] W. Casteels, J. Tempere, and J. T. Devreese, *J. Low Temp. Phys.* **162**, 266 (2011).
- [38] A. Härter, A. Krüchow, M. Deiß, B. Drews, E. Tiemann, and J. Hecker-Denschlag, *Nat. Phys.* **9**, 512 (2013).
- [39] A. Carrington, *Science* **274**, 1327 (1996).